



Universiteit  
Leiden  
The Netherlands

## Defect-mediated dynamics of coherent structures in active nematics

Serra, M.; Lemma, L.; Giomi, L.; Dogic, Z.; Mahadevan, L.

### Citation

Serra, M., Lemma, L., Giomi, L., Dogic, Z., & Mahadevan, L. (2023). Defect-mediated dynamics of coherent structures in active nematics. *Nature Physics*, 19(9), 1355-1361. doi:10.1038/s41567-023-02062-y

Version: Publisher's Version

License: [Licensed under Article 25fa Copyright Act/Law \(Amendment Taverne\)](#)

Downloaded from: <https://hdl.handle.net/1887/3718625>

**Note:** To cite this publication please use the final published version (if applicable).






# Defect-mediated dynamics of coherent structures in active nematics

Received: 3 April 2021

Accepted: 20 April 2023

Published online: 25 May 2023

 Check for updates

Mattia Serra <sup>1,2</sup> , Linnea Lemma<sup>3</sup>, Luca Giomi <sup>4</sup>, Zvonimir Dogic<sup>3</sup> & L. Mahadevan <sup>2,5,6</sup> 


Active fluids, such as cytoskeletal filaments, bacterial colonies and epithelial cell layers, exhibit distinctive orientational coherence, often characterized by nematic order and its breakdown, defined by the presence of topological defects. In contrast, little is known about positional coherence, that is, whether there is an organization in the underlying fluid motion—despite this being both a prominent and an experimentally accessible feature. Here we characterize the organization of fluid motion in active nematics using the notion of Lagrangian coherent structures by analyzing experimental data of two-dimensional mixtures of microtubules and kinesin, as well as numerical data obtained from the simulation of the active nematodynamic equations. Coherent structures consist of moving attractors and repellers, which orchestrate complex motion. To understand the interaction of positional and orientational coherence, we analyse experiments and simulations and find that  $+1/2$  defects move and deform the attractors, functioning as control centres for collective motion. Additionally, we find that regions around isolated  $+1/2$  defects undergo high bending and low stretching/shearing deformations, consistent with the local stress distribution. The stress is the minimum at the defect, whereas high differential stress along the defect orientation induces folding. Our work offers a new perspective to describe and control self-organization in active fluids, with potential applications to multicellular systems.

Many out-of-equilibrium systems, from bird flocks down to biofilms and the cell cytoskeleton, consist of agents that consume energy and self-organize into large-scale patterns and collectively moving structures<sup>1–9</sup>, which are breathtaking in their beauty and complexity and relevant for embryonic development, wound healing and cancer<sup>10–13</sup>. Understanding the mechanisms that lead to these patterns and characterizing the phases of active matter systems will unravel their complexity, suggesting ways to mimic them using synthetic materials and eventually control and design active systems using external fields.

Self-organized patterns are typically described in Eulerian coordinates, where the local velocity, pressure and orientation of the active building blocks are treated as fields within a fixed laboratory

frame. Two-point correlation functions, spectral densities and other quantities inspired by studies of statistical steady states of turbulence in Newtonian fluids, are typical outcomes of this approach<sup>14,15</sup>. Topological defects, that is, localized singularities in the orientation of the active building blocks<sup>2</sup>, have also been extensively studied and their dynamics are known to be inherently entangled with large-scale chaotic flows<sup>15–17</sup>. But what is the relation between the dynamics of defects and the large-scale coherent motion in flow fields that are typically spatially heterogeneous and temporally unsteady?

A natural framework to address this question is provided by the Lagrangian description of fluid flow. By tracing the motion of passive particles in unsteady flows, which may also include chaotic paths,

<sup>1</sup>Department of Physics, University of California San Diego, San Diego, CA, USA. <sup>2</sup>Paulson School of Engineering and Applied Sciences, Harvard University, Cambridge, MA, USA. <sup>3</sup>Department of Physics, University of California, Santa Barbara, Santa Barbara, CA, USA. <sup>4</sup>Instituut-Lorentz, Universiteit Leiden, Leiden, Netherlands. <sup>5</sup>Department of Organismic and Evolutionary Biology, Harvard University, Cambridge, MA, USA. <sup>6</sup>Department of Physics, Harvard University, Cambridge, MA, USA.  e-mail: [serram@ucsd.edu](mailto:serram@ucsd.edu); [lmahadev@g.harvard.edu](mailto:lmahadev@g.harvard.edu)

one can often identify robust skeletons, commonly referred to as coherent structures (CSs)<sup>18–20</sup>, which shape the trajectory patterns and reveal the organizing barriers to material transport<sup>21,22</sup>. Because we expect our results to hold regardless of the specific Lagrangian integration time, we will often use CSs, which include Lagrangian CSs<sup>18</sup> and their recently developed short-time limits<sup>19,23</sup>. Here we combine theoretical concepts from nonlinear dynamics, active nematodynamics simulations and experiments on suspensions of microtubules and kinesin to unravel the CSs underlying the chaotic flow of two-dimensional active nematics and their relation to the dynamics of topological defects.

## Results

### Lagrangian deformations and CSs

Our theoretical and computational framework for kinematic analysis starts by considering the velocity field  $\mathbf{v}(\mathbf{x}, t)$  of a planar active nematic fluid, and the corresponding flow map

$$\mathbf{F}_{t_0}^t(\mathbf{x}_0) = \mathbf{x}_0 + \int_{t_0}^t \mathbf{v}(\mathbf{F}_{t_0}^\tau(\mathbf{x}_0), \tau) d\tau. \quad (1)$$

This evolves the initial position  $\mathbf{x}_0$  of a virtual tracer particle to the corresponding position  $\mathbf{F}_{t_0}^t(\mathbf{x}_0)$  at time  $t$ , and its spatial derivatives describe the Lagrangian deformation of the nematic fluid over the time interval  $[t_0, t]$ . Locally, a small fluid patch can be stretched, sheared and folded. Stretching and shearing (Fig. 1) are completely characterized by the right Cauchy–Green strain tensor field  $\mathbf{C}_{t_0}^t(\mathbf{x}_0)$  (ref. 24) defined as

$$\mathbf{C}_{t_0}^t(\mathbf{x}_0) = \nabla \mathbf{F}_{t_0}^t(\mathbf{x}_0)^\top \nabla \mathbf{F}_{t_0}^t(\mathbf{x}_0), \quad (2)$$

where  $\nabla \mathbf{F}_{t_0}^t(\mathbf{x}_0)$  is the Jacobian of the flow map.

Given a material patch consisting of straight fibres at initial time (Fig. 1), we use the notation  $\lambda_1 \leq \lambda_2$  and  $\{\boldsymbol{\xi}_1, \boldsymbol{\xi}_2\}$  to denote the eigenvalues and the associated orthonormal eigenvectors of  $\mathbf{C}_{t_0}^t(\mathbf{x}_0)$ . Then one can interpret  $\boldsymbol{\xi}_2$  as the most stretched fibre (by a factor  $\sqrt{\lambda_2}$ ) and  $\boldsymbol{\xi}_1$  is the least stretched one (by a factor  $\sqrt{\lambda_1}$ ). In chaotic systems,  $\lambda_2$  usually grows exponentially in time, it is typically rescaled to read

$$A_{t_0}^t(\mathbf{x}_0) = \frac{1}{|t - t_0|} \log \sqrt{\lambda_2(\mathbf{x}_0)}, \quad (3)$$

which denotes the largest finite-time Lyapunov exponent (FTLE). The maximum stretching along  $\boldsymbol{\xi}_2$  implies that over long times, other fibres align with the local  $\boldsymbol{\xi}_2$  direction (Fig. 1), and follows from an asymptotic analysis of the underlying dynamical system<sup>25</sup>.

By contrast, folding deformations determine variations in the curvature of material fibres over time<sup>26</sup>. This effect can be computed from the second-order spatial derivatives of  $\mathbf{F}_{t_0}^t(\mathbf{x}_0)$  and provides additional information that complements notions of stretching and shearing characterized by first-order spatial derivatives. Starting with an infinitesimal patch of straight fibres at  $\mathbf{x}_0$ , from the  $\boldsymbol{\xi}_2$ -alignment property it follows that the most likely observable fluid folding, during the time interval  $[t_0, t]$ , is the one along the  $\boldsymbol{\xi}_2$  fiber (Fig. 1). This leads to a Lagrangian measure of folding relative to the initial fluid configuration, given by

$$\kappa_{t_0}^t(\mathbf{x}_0, \boldsymbol{\xi}_2) = \frac{[(\nabla^2 \mathbf{F}_{t_0}^t(\mathbf{x}_0) \boldsymbol{\xi}_2) \boldsymbol{\xi}_2] \cdot [\mathbf{R} \nabla \mathbf{F}_{t_0}^t(\mathbf{x}_0) \boldsymbol{\xi}_2]}{\lambda_2^{3/2}}, \quad (4)$$

where  $(\nabla^2 \mathbf{F}_{t_0}^t(\mathbf{x}_0) \boldsymbol{\xi}_2)_{ij} = \sum_k F_{t_0,ijk}^t(\mathbf{x}_0) \boldsymbol{\xi}_{2k}$ ,  $i, j, k \in \{1, 2\}$  and  $\mathbf{R}$  denotes a counterclockwise 90°-rotation matrix (Supplementary Section 1). Analogously, the same folding can be represented at the final

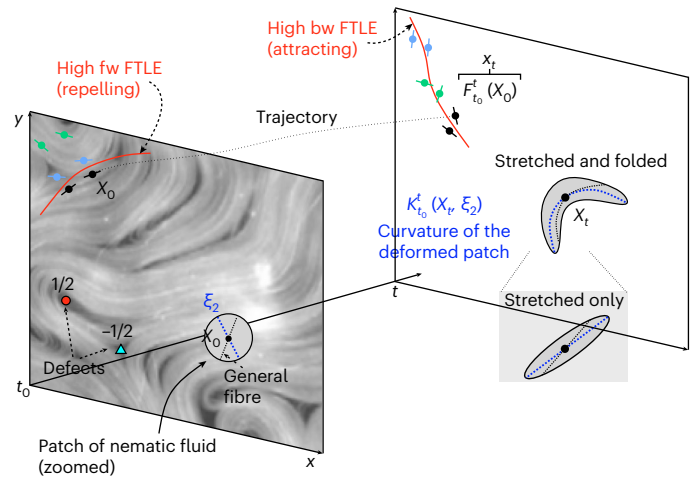


**Fig. 1 | Lagrangian view of an active nematic fluid.** The red curves demarcate the repelling and attracting regions in the flow identified by large values of the forward and backward FTLE. The repellers are based on the initial fluid configuration, whereas the attractors are based on the final configuration. Initially close tracers that are on opposite sides of a forward FTLE ( $\mathcal{A}$ ) ridge will move far apart at time  $t$ . Similarly, initially distant tracers are attracted to a backward FTLE ( $\mathcal{A}$ ) ridge at time  $t$ . Moreover an infinitesimal patch of nematic fluid at  $\mathbf{x}_0$  will get stretched and folded over the time interval  $[t_0, t]$ . Different fibres in this patch tend to align along the fiber  $\boldsymbol{\xi}_2(\mathbf{x}_0)$  corresponding to the maximally stretched direction, and the curvature of the folded patch is  $\kappa_{t_0}^t(\mathbf{x}_t, \boldsymbol{\xi}_2)$ .

position  $\mathbf{x}_t$  by transporting the curvature along the flow trajectories (Fig. 1), so that

$$\kappa_{t_0}^t(\mathbf{x}_t, \boldsymbol{\xi}_2) = \kappa_{t_0}^t(\mathbf{F}_{t_0}^t(\mathbf{x}_0), \boldsymbol{\xi}_2). \quad (5)$$

Large values of  $\kappa_{t_0}^t(\mathbf{x}_0, \boldsymbol{\xi}_2)$  mark the initial positions  $\mathbf{x}_0$  of the nematic fluid that will undergo large folding in the time interval  $[t_0, t]$ , and similarly,  $\kappa_{t_0}^t(\mathbf{x}_t, \boldsymbol{\xi}_2)$  identifies the final positions of the nematic fluid that experience small/large curvature changes (in the Supplementary Section 1, we provide general expressions for the material curvature and its alternative formulation in terms of Eulerian quantities such as flow vorticity, divergence and rate-of-strain tensor). Altogether, equations (3)–(5) completely quantify the maximum stretching and folding deformations of a continuum moving under a given flow map  $\mathbf{F}_{t_0}^t$ . These kinematic measures are model independent and agnostic to the mechanisms driving the flow; hence they are applicable to experimental and computational velocity fields of arbitrary origin and are readily implementable.

In terms of these measures, we can interpret the forward FTLE (fw FTLE or  $\mathcal{A}$ ) as a scalar field over the initial particle positions  $\mathbf{x}_0$  that quantifies the maximum local deformation and identifies the location of maximum spatial separation of initially close particles over the time interval  $[t_0, t]$ . Similarly, the backward FTLE (bw FTLE or  $\mathcal{A}$ ), defined over the final positions  $\mathbf{x}_t$ , identifies the location of the maximum spatial convergence of initially distant particles over  $[t_0, t]$ . Together, they demarcate regions of attraction (attracting CS) and repulsion (repelling CS) (Fig. 1). Despite the fact that FTLE ridges are rarely not material<sup>18</sup>, here we adopt FTLE-based CSs, instead of geodesic ones<sup>18,19</sup>, because we are interested in attraction and repulsion due to both shear and normal deformations, and FTLE CSs are simpler than geodesic CSs to compute and analyse.

### CSs organize particle motion

We now employ these analytical tools to analyse experimental observations of two-dimensional microtubule-based active nematic liquid crystals assembled on a surfactant-stabilized oil–water interface<sup>27</sup>.

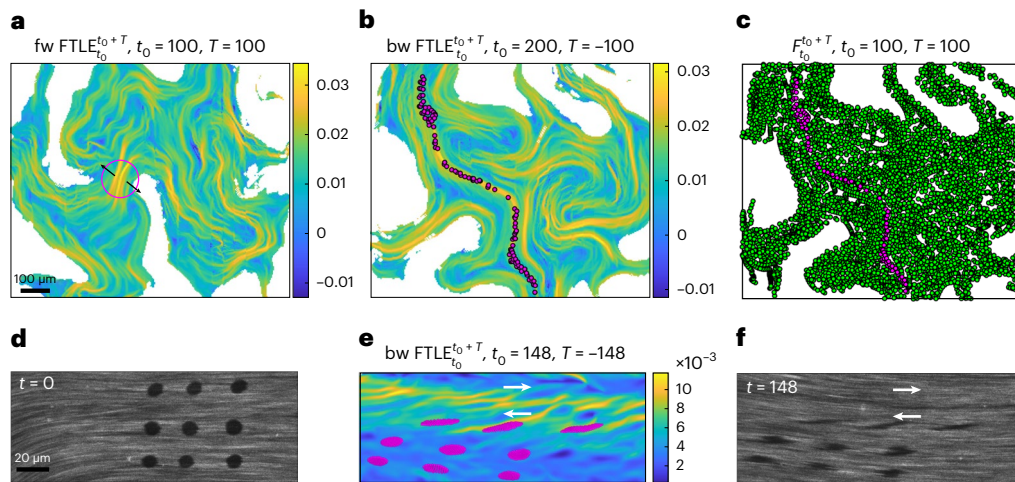


**Fig. 2 | Dynamics of a two-dimensional microtubule-based extensile active nematic system assembled on an oil–water interface.** The PIV based velocity is reconstructed on a uniform  $670 \times 800 \mu\text{m}^2$  grid with a spatial resolution of  $15.6 \mu\text{m}$  and temporal resolution of 1 frame per second. **a**,  $\rho A$  field whose ridges mark repelling CSs. The white regions demarcate the set of particles that left the domain where the velocity field is available. **b**,  $\rho A$  field whose ridges mark attracting CSs. The magenta dots represent the final ( $t = 200$ ) position of the tracers that started inside the magenta circle (shown in **a**) at the initial time  $t = 100$ . **c**, Final position of the tracers that started from a uniform grid at the

initial time. The particles that started outside the magenta circle are indicated in green; see Supplementary Video 1. **d–f**, Fluorescence recovery after photobleaching experiment in active nematics. Initial and final configuration of the fluorescence recovery after photobleaching experiment (**d** and **f**). **e**, The FTLE  $\rho A_{148}^0$  along with advected particles at  $t = 148$ , initialized to correspond to the photobleached regions at  $t = 0$ . Supplementary Video 2 shows the data in **d** and **e** for increasing  $t$ . Time is indicated in seconds (s). The colour bars encode the attraction or repulsion rates (in  $\text{s}^{-1}$ ). In **d–f**, the ATP concentration is  $18 \mu\text{M}$ .

The large-scale chaotic dynamics of these materials is collectively driven by kinesin molecular motors that move along multiple filaments to induce relative filament sliding.

Using particle image velocimetry (PIV), we reconstruct the velocity field of autonomously flowing active nematics. Supplementary Section 2 and Supplementary Figs. 1 and 2 provide details of the PIV-derived velocity and its validation for computing the Lagrangian trajectories. From the velocity field, we compute  $\rho A$  and  $\rho A$  for different timescales  $|T| = |t - t_0|$  using equations (1)–(3). Figure 2a,b shows the  $\rho A$  and  $\rho A$  fields for  $|T| = 100$  s. As sketched in Fig. 1, particles are repelled from a  $\rho A$  ridge and attracted towards a  $\rho A$  ridge (covered by magenta dots). Figure 2c shows the final position of a set of particles initially released from a uniform grid and serves as a tracker of particle motion. Supplementary Video 1 shows the time evolution of the FTLE fields and particle positions. Although the active fluid seems to move chaotically, there is an underlying coherent skeleton, captured by the FTLE fields, that dynamically organizes their motion but remains inaccessible from the mere inspection of fluid tracers.

The FTLE also provides a  $|T|$ -dependent map of the stretching and shearing Lagrangian deformation of the active continuum, with ridges that demarcate sets of the fluid that will experience higher deformations relative to their neighbours. Along the trajectories, the Lagrangian deformation consistently integrates the separate contributions of viscous, elastic and active stresses deforming the nematic fluid and thus encodes a memory trace of the nematodynamic field.

To correlate these computed Lagrangian memory traces with direct observations of the deformation patterns near  $\rho A$  ridges, we label the regions of microtubule-based active nematics and observe their subsequent evolution (Supplementary Section 2). This is achieved by photobleaching nine circular regions with a radius of  $\sim 4 \mu\text{m}$  (Fig. 2d). Using the PIV data, we compute the  $\rho A$  field along with the position of Lagrangian tracers (magenta) initialized at  $t = 0$  in correspondence with the photobleached regions (Fig. 2e). Stripe-shaped ridges of  $\rho A_{148}^0$  reveal a horizontal shear layer, along with regions of distinctly high attraction and Lagrangian deformations. Our analysis predicts the

evolution of advected and diffused photobleached patches (Fig. 2f and Supplementary Video 2). Overall,  $\rho A_{148}^0$  provides a  $|T|$ -dependent map of attraction as well as stretching and shearing deformations maps over the entire domain.

### Positive defects mediate attracting CSs

Having uncovered the organizers of the flow fields using Lagrangian CSs, we now turn to understand if and how they are related to the visible dynamics of topological defects, well known to be correlated with complex, large-scale nematodynamic flows<sup>15,17</sup>. To enable this, we redid our experiments with the microtubule–kinesin system, slowed the dynamics by reducing ATP concentration to  $2 \mu\text{M}$  and simultaneously measured both velocity  $\mathbf{v}$  and nematic director  $\mathbf{n}$  fields (Supplementary Section 2).

We mark  $+1/2$  defects with red dots and  $-1/2$  defects with cyan triangles (Fig. 1). Figure 3a–c shows  $\rho A$  for increasing time intervals, along with the positions of tracers (magenta), initially released from a circular blob and eventually attracted to a  $\rho A$  ridge. Supplementary Video 3 shows the time evolution of  $\rho A$  and  $\rho A$  along with particle positions. The FTLE fields again uncover the organizers of fluid motion that are inaccessible to trajectory plots alone.

Along with  $\rho A$ , Fig. 3a–c shows the evolution of topological defects, with the red arrows indicating the direction of motion of positive defects. These data suggest that positive defects move and deform  $\rho A$  ridges, which, in turn, directs particle motion. Displaying the director field with the  $\rho A$  field (Fig. 3c) shows that  $\mathbf{n}$  aligns with the  $\rho A$  ridges, suggesting that the director tends to align with the direction of maximum stretching<sup>17</sup>. The entire time evolution of  $\mathbf{n}$  and  $\rho A$  is shown in Supplementary Video 3 (middle). Interestingly,  $+1/2$  defects appear to be in regions of low Lagrangian stretching or shearing deformation as quantified by the FTLE field. By contrast, the Lagrangian folding measure is maximum at the defects (Fig. 3d), where the absolute folding field  $|\kappa_{t_0}^c(\mathbf{x}_t, \boldsymbol{\xi}_2)|$  is superimposed to the nematic director  $\mathbf{n}$  at the same time as that in Fig. 3a.

To further quantify our observations on deformations at defects and the correlation of their dynamics with the FTLE  $\rho A$ , next we turn to numerical simulations of an incompressible ( $\nabla \cdot \mathbf{v} = 0$ ) planar uniaxial

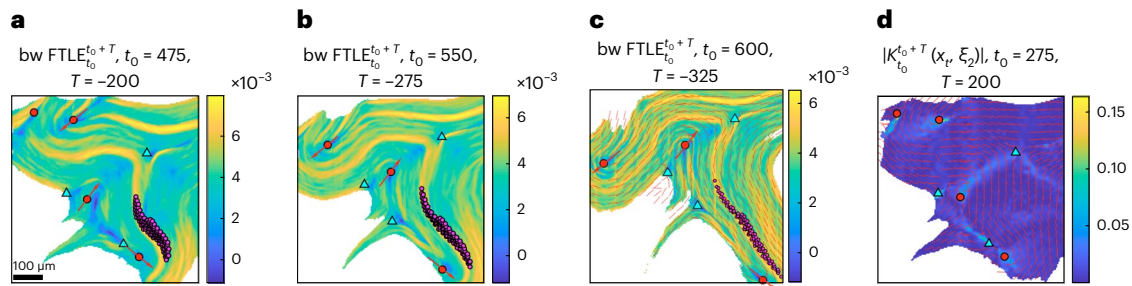


**Fig. 3 | Dynamics of an extensile active suspension of microtubule bundles and kinesin at an oil-water interface with a 2  $\mu\text{M}$  ATP concentration.** **a**,  $\nu A$  for  $|T| = 200$  s along with the position of tracers (magenta) attracted to a  $\nu A$  ridge and initially released from a circular blob. **b, c**, Same as **a** but for larger  $|T|$ . The red arrows illustrate  $+1/2$  defects pulling at the attracting  $\nu A$  ridges that, in turn, shape the Lagrangian particle motion. **d**, Absolute folding field  $|\kappa_{t_0}^{\xi_1, \xi_2}(x_t, \xi_2)|$  for

$T = 200$  s, along with topological defects and director field at the current time  $t_0 + T$  as in **a**. Defects are invariably located at regions of high folding and low stretching or shearing Lagrangian deformation. In **c** and **d**, the director field  $\mathbf{n}$  is shown in red. Time is in seconds. The colour bar in **d** encodes the Lagrangian folding in  $1 \mu\text{m}^{-1}$ , whereas the attraction rates are shown in  $\text{s}^{-1}$ . Supplementary Video 3 shows the time evolution of  $\nu A$  and  $\nu A$  along with particle motions.

active nematic liquid crystal whose dynamics are given by the nematodynamic equations

$$\rho \frac{d\mathbf{v}}{dt} = -\nabla p + \eta \nabla^2 \mathbf{v} + \nabla \cdot (\boldsymbol{\sigma}^e + \boldsymbol{\sigma}^a), \quad (6a)$$

$$\frac{d\mathbf{Q}}{dt} = \lambda \mathbf{S} \mathbf{D} + \mathbf{Q} \boldsymbol{\Omega} - \boldsymbol{\Omega} \mathbf{Q} + \gamma^{-1} \mathbf{H}, \quad (6b)$$

which can be derived from phenomenological arguments or microscopic models, and capture typical experimental statistics<sup>15</sup>. Here  $\rho$  and  $\eta$  denote the density and viscosity of the nematic fluid, respectively;  $d/dt = \partial_t + \mathbf{v} \cdot \nabla$  is the material derivative;  $\lambda$  is the flow alignment parameter; and  $\gamma$  is the rotational viscosity<sup>28</sup>. In equation (6b),  $\mathbf{Q} = S(\mathbf{n} \otimes \mathbf{n} - \mathbf{I}/2)$  denotes the nematic tensor,  $0 \leq S \leq 1$  is the nematic order parameter,  $\mathbf{I}$  is the identity tensor,  $\mathbf{D} = [\nabla \mathbf{v} + (\nabla \mathbf{v})^T]/2$  is the symmetric part and  $\boldsymbol{\Omega} = [\nabla \mathbf{v} - (\nabla \mathbf{v})^T]/2$  is the antisymmetric part of the velocity gradient  $\nabla \mathbf{v}$ .  $\mathbf{H} = -\delta F/\delta \mathbf{Q} = K \nabla^2 \mathbf{Q}^2 - (a_2 + a_4 |\mathbf{Q}|^2) \mathbf{Q}$  is the molecular tensor governing the relaxation dynamics of the nematic phase defined as the variational derivative of the two-dimensional Landau-De Gennes free energy  $F = \int f dA$ , where  $f$ , the free-energy density, is<sup>28</sup>

$$f = \frac{1}{2} K |\nabla \mathbf{Q}|^2 + \frac{1}{2} a_2 |\mathbf{Q}|^2 + \frac{1}{4} a_4 |\mathbf{Q}|^4, \quad (7)$$

where  $|\cdot|$  denotes the Frobenius norm (that is,  $|\mathbf{Q}|^2 = Q_{ij} Q_{ij}$ ),  $K$  is the orientational stiffness relating the elastic free energy to spatial inhomogeneities in the configuration of the nematic tensor and  $a_2$  and  $a_4$  are the bulk moduli. Finally,  $\boldsymbol{\sigma}^e = -\lambda \mathbf{S} \mathbf{H} + \mathbf{Q} \mathbf{H} - \mathbf{H} \mathbf{Q}$  denotes the elastic stress arising from a departure from the lowest free-energy configuration and  $\boldsymbol{\sigma}^a = \alpha \mathbf{Q}$  is the contractile ( $\alpha > 0$ ) or extensile ( $\alpha < 0$ ) active stress exerted by the active particles along  $\mathbf{n}$ . We non-dimensionalize distances by the length scale  $\ell = L/5$ , where  $L$  is the system size, time by the viscous timescale  $\tau = \rho \ell^2/\eta$  and energy by  $\varepsilon = K$ . Since the typical Reynolds number of microtubules/kinesin suspensions varies in the range of  $10^{-5}$ – $10^{-3}$  depending on the ATP concentration, we eliminate the convective derivative in equation (6a) and numerically integrate equations (6a) and (6b) using finite differences on a  $128 \times 128$  collocated grid with periodic boundary conditions. Following<sup>15</sup>, we select our parameters so that the nematodynamic flows are turbulent and show that our results apply even to chaotic regimes. In all our simulations, we set the parameter values as follows:  $\lambda = 0.1$ ,  $K = 1$ ,  $a_2 = -1$ ,  $a_4 = 2$ ,  $\gamma = 10$ ,  $\alpha = -25$  and  $L = 5$ , in previously defined rescaled units (Supplementary Section 3 provides the selection of parameters). This yields the velocity field  $\mathbf{v}$  along with the nematic tensor field  $\mathbf{Q}$ , from which we identify the topological defects

(Supplementary Section 4). Our results apply to both contractile and extensile cases. We show extensile experimental and numerical datasets in the main text and contractile active nematics in the Supplementary Information.

Figure 4a–c shows  $\nu A$  for different time intervals  $|T|$ , along with the position of an initially circular set of particles (magenta) that are attracted to a  $\nu A$  ridge. Analogous to our results of the analysis of the experiments, we find that  $\nu A$  ridges are pulled (red arrows) and shaped by moving Eulerian  $+1/2$  defects and remain insensitive to  $-1/2$  defects (Fig. 4a–c). In Supplementary Section 4 and Supplementary Fig. 3, we quantify the correlation between the evolution of  $\nu A$  and defect motion. We first find a velocity field that transports and deforms  $\nu A$  over increasing  $T$ , and evaluate it at defects. The  $\nu A$  evolution along with defect velocities are provided in Supplementary Video 5. We then compute the relative angle between the  $\nu A$  velocity at defects and defects velocities. The mean and standard deviation of the relative angle associated with positive defects are six times smaller compared to those related to negative defects. We perform the same analysis on the experimental data in Fig. 3 and find that the mean and standard deviation of the relative angle associated with positive defects are three and four times smaller, respectively, compared with those related to negative defects (Supplementary Section 4). Supplementary Video 6 is similar to Supplementary Video 5 but for the experimental data. We note that  $\nu A$  is Lagrangian, that is, it contains information of particle trajectories, whereas defects are Eulerian and hence agnostic to particle paths. This connection could provide a quantitative framework to control the Lagrangian motion and deformation of active nematics by steering the position of Eulerian defects.

As in Fig. 3c, Fig. 4c shows that  $\mathbf{n}$  tends to align with attracting  $\nu A$  ridges. By contrast, in contractile active nematics simulated using equations (6a) and (6b) with the same parameters of the extensile case and  $\alpha = 25$ , we find that  $\mathbf{n}$  tends to be perpendicular to attracting  $\nu A$  ridges (Supplementary Section 5 and Supplementary Fig. 4). In Supplementary Section 6 and Supplementary Fig. 5, we perform the same analysis as that in Fig. 4 on simulated extensile active nematic in confined geometry characterized by dancing defects<sup>29</sup> and find again that  $\mathbf{n}$  tends to align with attracting  $\nu A$  ridges, consistent with Figs. 3c and 4c. In Supplementary Section 7 and Supplementary Fig. 6, we provide a mechanistic argument that explains these observations. First, we show that in extensile (contractile) nematics,  $\mathbf{n}$  tends to align with (perpendicular to) the leading eigenvector  $\mathbf{e}_2$  of  $\mathbf{D}$ . This provides a precise connection between  $\mathbf{n}$  and Eulerian—or short-time—attractors (repellers)<sup>19</sup>, which are parallel (perpendicular) to  $\mathbf{e}_2$ . Then, we relate  $\mathbf{n}$  to Lagrangian attractors.

In Supplementary Section 8 and Supplementary Fig. 7, we also provide an aggregate measure of positional coherence by

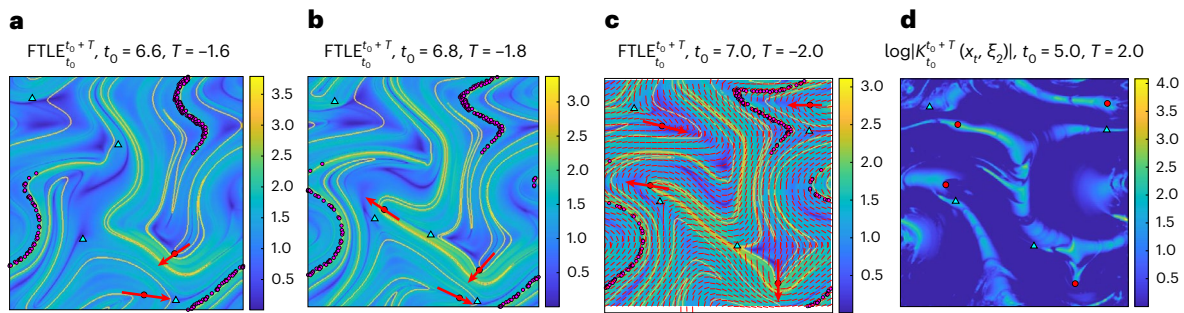


**Fig. 4 | Lagrangian analysis of a simulated extensile active nematic fluid.** The nematic fluid obeys equations (6a) and (6b). **a**,  $\mathcal{L}A$  for  $|T| = 1.6$ , along with the position of material particles (magenta) attracted to a  $\mathcal{L}A$  ridge and initially released from a circular blob. **b, c**, Same as **a**, but for larger  $|T|$ . The red arrows illustrate that  $+1/2$  defects pull the attracting  $\mathcal{L}A$  ridges that, in turn, shape particle

motion. In **c**, the red segments display the director field. **d**, Logarithm of the folding field modulus  $|K_{t_0}^{t_0+T}(x_t, \xi_2)|$  for  $T = 2$ , as that in **c**. Supplementary Video 4 shows the evolution of the data in **a** and **d** for different  $T$  values. The positive defects are located at regions of high folding and low stretching or shearing Lagrangian deformation.

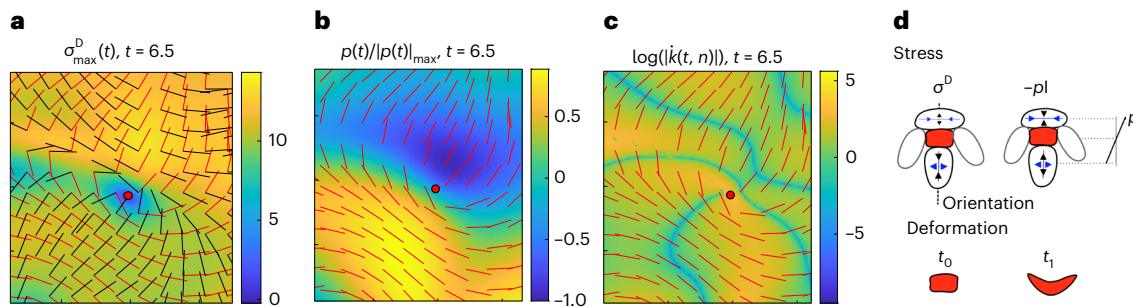


**Fig. 5 | Stress and deformation around an isolated  $+1/2$  defect in simulated extensile active nematics.** **a**, Maximum eigenvalue of the total deviatoric stress  $\sigma^D$  in the proximity of a  $+1/2$  defect (red circle). The leading eigenvector of  $\sigma^D$  is marked by black lines and the the nematic director field, by red lines (Supplementary Fig. 10 shows separate viscous, elastic and active stress contributions). **b**, Pressure field normalized by its maximum absolute value characterizes the isotropic stress  $\sigma^I = -pl$ . **c**, Logarithm of the folding rate

modulus of the active nematic, computed from equation (8). **d**, Sketch of the deviatoric and isotropic stress distribution near an isolated  $+1/2$  defect in extensile active nematics (top). The arrow size is proportional to the stress level, and the blue arrow marks the direction perpendicular to defect orientation. A sketch of the material deformation near a  $+1/2$  defect (bottom). Supplementary Fig. 9 shows the equivalent analysis for the contractile case.

using the inverse of the broadly used  $H^{-1}$  mixing norm<sup>30</sup>, and show how it decreases with increasing integration time  $T$  and activity  $\alpha$ . Our results are consistent with<sup>17</sup> where it was discovered that in the asymptotic limit  $T \rightarrow \infty$ , the braiding of positive defects contributes dominantly to the increase in topological entropy in active nematics. However, although<sup>17</sup> quantifies the contribution of  $+1/2$  defects to the aggregate (that is, space-independent) mixing, here we focus and uncover dynamic spatial structures (attracting Lagrangian CSs) that shape particle motion while being steered by  $+1/2$  defects. In other words, we identify the spatiotemporal organizer of active nematics that complement previous analyses of global mixing properties. Figure 4d shows  $\kappa_{t_0}^t(x_t, \xi_2)$  associated with  $|T| = 2$  (Fig. 4c). Consistent with our experimental results (Fig. 3), we see that  $+1/2$  defects are preferentially located in regions of high Lagrangian folding and low stretching. We obtain results similar to Fig. 4 for contractile ( $\alpha > 0$ ) active nematics, simulated using the same parameters listed above and  $\alpha = 25$  (Supplementary Section 5). Supplementary Video 7 shows the same data as Supplementary Video 4 but for the contractile case. Finally, in Supplementary Section 9 and Supplementary Fig. 8, we confirm that Lagrangian structures contained in  $\mathcal{L}A$  and  $\kappa$  remain typically inaccessible to Eulerian quantities such as the director field  $\mathbf{n}$ , the nematic order parameter  $S$ , the eigenvalues and eigenvectors of the rate-of-strain tensor, the velocity divergence  $\nabla \cdot \mathbf{v}$ , and bend and splay elastic energies.

**Stress gradients are maximum at positive defects**

Motivated by the striking deformations associated with  $+1/2$  defects, we analyse the stress distribution using the simulation data for extensile active nematics in Fig. 4. We find that the magnitude of both deviatoric and isotropic total stresses are minimum at  $+1/2$  defects, but their gradients have high values at these locations along the defect orientation (Fig. 5a,b), and thus induces folding deformation (Fig. 5d). We obtain similar results for contractile active nematics (Supplementary Section 10 and Supplementary Fig. 9), where the folding direction is towards the head of the defect as opposed to the tail (Fig. 5d).

To bridge the gap between the Lagrangian deformations, which accounts for the motion history of the nematic continuum, and Eulerian deformations based on an instantaneous configuration, we derived an exact formula for the Eulerian folding rate

$$\dot{\kappa}(t, \mathbf{x}, \mathbf{n}) = [(\mathbf{VD}(\mathbf{x}, t)\mathbf{n})\mathbf{n}] \cdot \mathbf{n}_1 - \frac{\nabla\omega(\mathbf{x}, t) \cdot \mathbf{n}}{2} \quad (8)$$

experienced by an infinitesimal patch of nematic fluid with orientation  $\mathbf{n}$  (Supplementary Section 1). The folding rate can be computed from  $\mathbf{v}$  and  $\mathbf{n}$ , and arises from spatial heterogeneities of the rate-of-strain tensor  $\mathbf{D}$  and vorticity  $\omega$ . For example, if the nematic continuum is an epithelium,  $\dot{\kappa}(t, \mathbf{x}, \mathbf{n})$  measures the bending rate experienced by the cell located at  $\mathbf{x}$  with orientation  $\mathbf{n}$ . Using equation (8), we also find

that  $k(t, \mathbf{x}, \mathbf{n})$  is the maximum in the vicinity of +1/2 defects (Fig. 5c), consistent with the corresponding stress distribution (Fig. 5a,b) and Lagrangian folding (Fig. 4).

It is interesting to compare these results with experimental findings that suggest a biological consequence of topological defects in epithelial layers<sup>12,31,32</sup>, where the deformations and stress at the defects is thought to elucidate how mechanical stimuli are converted into downstream biochemical signals. Positive defects with strength +1/2 in monolayers of Madin–Darby canine kidney cells, for example, have been associated with sites of cell apoptosis<sup>31</sup>, with a possible explanation being the high compressive stress at the defect location. This hypothesis has been tested by correlating the isotropic stress averaged over several (~6) cell sizes in the neighbourhood of a topological defect during apoptosis<sup>31</sup>. Our findings, however, show that bending deformations are dominant at positive defects, suggesting that there may be other mechanisms at play associated with bending deformations at topological defects.

We observe a clear similarity of the extensile active nematic stress distribution (Fig. 5) with that experimentally measured in monolayers of Madin–Darby canine kidney cells<sup>31</sup> during apoptosis. It is worth noting that the novel stress and deformation distribution around +1/2 defects, together with the known ability of cells to sense curvature changes<sup>33</sup>, may lead to uncovering new feedback mechanisms in active epithelial dynamics<sup>34,35</sup>.

## Discussion

By combining concepts from nonlinear dynamics, experiments on two-dimensional active nematics, and simulations of active nematodynamics equations, we found that the motion of active nematics is organized by dynamic (time-dependent) attracting and repelling CSs, whose motion is coupled to that of +1/2 topological defects. As the defects move, they deform attracting CSs, which in turn regulate collective motion. Furthermore, the Lagrangian timescale-dependent maps of stretching- and folding-type deformations of a nematic continuum show that +1/2 defects are correlated with locations of high bending and low stretching-type or shearing-type deformations. Motivated by this finding, we have discovered a characteristic stress distribution around +1/2 defects: the stress is the minimum at the defect, but its large gradient along the defect's orientation causes differential stress that induces bending. The bending is towards the defect head (tail) for contractile (extensile) active nematics. Similar stress distributions were experimentally measured in monolayers of Madin–Darby canine kidney cells<sup>31</sup>. Finally, we have observed and explained that the nematic director tends to align along (perpendicular to) attracting Eulerian and Lagrangian CSs<sup>18,19</sup> for extensile (contractile) active nematics.

More broadly, using only the measured velocity and nematic director, our results provide a quantitative framework for assessing the motion, mixing and deformation of active nematics. Emerging experimental evidence associates biological functionality with topological defects of cells orientation<sup>12</sup>, actin fibre orientation<sup>36</sup> and the ability of cells to sense and react to bending and stretching deformations<sup>33</sup>. From this perspective, our approach quantifies the stretching and folding deformations in a nematic continuum as timescale-dependent maps. Investigating the correlation between curvature and stretching deformation maps in epithelial layers and other similar systems could elucidate how cells couple mechanical inputs to intracellular signals in oriented active matter systems.

## Online content

Any methods, additional references, Nature Portfolio reporting summaries, source data, extended data, supplementary information, acknowledgements, peer review information; details of author contributions and competing interests; and statements of data and code availability are available at <https://doi.org/10.1038/s41567-023-02062-y>.

## References

- Vicsek, T. & Zafeiris, A. Collective motion. *Phys. Rep.* **517**, 71–140 (2012).
- Marchetti, M. C. et al. Hydrodynamics of soft active matter. *Rev. Mod. Phys.* **85**, 1143–1189 (2013).
- Kruse, K., Joanny, J., Jülicher, F., Prost, J. & Sekimoto, K. Asters, vortices, and rotating spirals in active gels of polar filaments. *Phys. Rev. Lett.* **92**, 078101 (2004).
- Ballerini, M. et al. Interaction ruling animal collective behavior depends on topological rather than metric distance: evidence from a field study. *Proc. Natl Acad. Sci. USA* **105**, 1232–1237 (2008).
- Zhang, H., Ber, A., Florin, E. & Swinney, H. Collective motion and density fluctuations in bacterial colonies. *Proc. Natl Acad. Sci. USA* **107**, 13626–13630 (2010).
- Bricard, A., Caussin, J., Desreumaux, N., Dauchot, O. & Bartolo, D. Emergence of macroscopic directed motion in populations of motile colloids. *Nature* **503**, 95–98 (2013).
- Dombrowski, C., Cisneros, L., Chatkaew, S., Goldstein, R. & Kessler, J. Self-concentration and large-scale coherence in bacterial dynamics. *Phys. Rev. Lett.* **93**, 098103 (2004).
- Copenhagen, K., Alert, R., Wingreen, N. S. & Shaevitz, J. W. Topological defects promote layer formation in *Myxococcus xanthus* colonies. *Nat. Phys.* **17**, 211–215 (2021).
- Meacock, O. J., Doostmohammadi, A., Foster, K. R., Yeomans, J. M. & Durham, W. M. Bacteria solve the problem of crowding by moving slowly. *Nat. Phys.* **17**, 205–210 (2021).
- Fiedl, P. & Gilmour, D. Collective cell migration in morphogenesis, regeneration and cancer. *Nat. Rev. Mol. Cell Biol.* **10**, 445–457 (2009).
- Ladoux, B. & Mège, R. Mechanobiology of collective cell behaviours. *Nat. Rev. Mol. Cell Biol.* **18**, 743–757 (2017).
- Doostmohammadi, A., Ignés-Mullol, J., Yeomans, J. & Sagués, F. Active nematics. *Nat. Commun.* **9**, 3246 (2018).
- Serra, M., Streichan, S., Chuai, M., Weijer, C. J. & Mahadevan, L. Dynamic morphoskeletons in development. *Proc. Natl Acad. Sci. USA* **117**, 11444–11449 (2020).
- Wensink, H. et al. Meso-scale turbulence in living fluids. *Proc. Natl Acad. Sci. USA* **109**, 14308–14313 (2012).
- Giomí, L. Geometry and topology of turbulence in active nematics. *Phys. Rev. X* **5**, 031003 (2015).
- Shankar, S. & Marchetti, M. C. Hydrodynamics of active defects: from order to chaos to defect ordering. *Phys. Rev. X* **9**, 041047 (2019).
- Tan, A. J. et al. Topological chaos in active nematics. *Nat. Phys.* **15**, 1033–1039 (2019).
- Haller, G. Lagrangian coherent structures. *Annu. Rev. Fluid Mech.* **47**, 137–162 (2015).
- Serra, M. & Haller, G. Objective Eulerian coherent structures. *Chaos* **26**, 053110 (2016).
- Hadjighasem, A., Farazmand, M., Blazeviski, D., Froyland, G. & Haller, G. A critical comparison of Lagrangian methods for coherent structure detection. *Chaos* **27**, 053104 (2017).
- Serra, M., Sathe, P., Beron-Vera, F. & Haller, G. Uncovering the edge of the polar vortex. *J. Atmos. Sci.* **74**, 3871–3885 (2017).
- Serra, M. et al. Search and rescue at sea aided by hidden flow structures. *Nat. Commun.* **11**, 2525 (2020).
- Nolan, P. J., Serra, M. & Ross, S. D. Finite-time Lyapunov exponents in the instantaneous limit and material transport. *Nonlinear Dyn.* **100**, 3825–3852 (2020).
- Truesdell, C. & Noll, W. *The Non-Linear Field Theories of Mechanics* (Springer, 2004).
- Giona, M. & Adrover, A. Nonuniform stationary measure of the invariant unstable foliation in Hamiltonian and fluid mixing systems. *Phys. Rev. Lett.* **81**, 3864 (1998).
- Serra, M., Vétel, J. & Haller, G. Exact theory of material spike formation in flow separation. *J. Fluid Mech.* **845**, 51–92 (2018).

27. Sanchez, T., Chen, D., DeCamp, S., Heymann, M. & Dogic, Z. Spontaneous motion in hierarchically assembled active matter. *Nature* **491**, 431–434 (2012).
28. De Gennes, P. & Prost, J. *The Physics of Liquid Crystals* 2nd edn (Oxford Univ. Press, 1993).
29. Shendruk, T. N., Doostmohammadi, A., Thijssen, K. & Yeomans, J. M. Dancing disclinations in confined active nematics. *Soft Matter* **13**, 3853–3862 (2017).
30. Doering, C. R. & Thiffeault, J.-L. Multiscale mixing efficiencies for steady sources. *Phys. Rev. E* **74**, 025301 (2006).
31. Saw, T. et al. Topological defects in epithelia govern cell death and extrusion. *Nature* **544**, 212–216 (2017).
32. Kawaguchi, K., Kageyama, R. & Sano, M. Topological defects control collective dynamics in neural progenitor cell cultures. *Nature* **545**, 327–331 (2017).
33. Dreher, D., Pasakarnis, L. & Brunner, D. Snapshot: mechanical forces in development II. *Cell* **165**, 1028–1028 (2016).
34. Aragona, M. et al. A mechanical checkpoint controls multicellular growth through YAP/TAZ regulation by actin-processing factors. *Cell* **154**, 1047–1059 (2013).
35. Balasubramaniam, L. et al. Investigating the nature of active forces in tissues reveals how contractile cells can form extensile monolayers. *Nat. Mater.* **20**, 1156–1166 (2021).
36. Maroudas-Sacks, Y. et al. Topological defects in the nematic order of actin fibres as organization centres of hydra morphogenesis. *Nat. Phys.* **17**, 251–259 (2021).

**Publisher's note** Springer Nature remains neutral with regard to jurisdictional claims in published maps and institutional affiliations.

Springer Nature or its licensor (e.g. a society or other partner) holds exclusive rights to this article under a publishing agreement with the author(s) or other rightsholder(s); author self-archiving of the accepted manuscript version of this article is solely governed by the terms of such publishing agreement and applicable law.

© The Author(s), under exclusive licence to Springer Nature Limited 2023



## Methods

### Experimental data

We discuss our microtubule-based active nematic experiments in detail in Supplementary Section 2.

### Numerical data

We solve our active nematodynamic equations using a dedicated code developed elsewhere<sup>15</sup>.

### FTLE, Lagrangian folding and Eulerian folding rates

Given a modelled or experimental planar velocity field  $\mathbf{v}(\mathbf{x}, t)$ , we compute the Lagrangian attractors and repellers from backward and forward FTLE (equation (3)). To compute the FTLE, we first calculate  $\mathbf{F}_{t_0}^t(\mathbf{x}_0)$  (equation (1)) by integrating the cell velocity field  $\mathbf{v}(\mathbf{x}, t)$  using the built-in Runge–Kutta solver ODE45 in MATLAB 2021b with absolute and relative tolerance of  $10^{-6}$ , linear interpolation in space and time and a uniform dense grid of initial conditions. Then, we compute  $\nabla\mathbf{F}_{t_0}^t(\mathbf{x}_0)$  taking the spatial derivatives of  $\mathbf{F}_{t_0}^t(\mathbf{x}_0)$  with respect to the initial conditions using centred finite-difference approximation. Using equation (2), we compute  $\mathbf{C}_{t_0}^t(\mathbf{x}_0)$  and use the eigenvalue MATLAB function to calculate its largest eigenvalue field  $\lambda_2$  and the corresponding eigenvector field  $\boldsymbol{\xi}_2$ . Using numerical centred finite differencing, we calculate the second spatial derivatives of  $\mathbf{F}_{t_0}^t(\mathbf{x}_0)$  and compute the Lagrangian folding field  $\kappa$  from equation (4). Using the same numerical schemes, we compute the Eulerian folding rate field  $\dot{\kappa}$  (equation (8)).

### Topological defects

We discuss the identification of topological defects, calculation of defect velocity and their correlation with the motion of Lagrangian attractors in detail in Supplementary Section 4.

### Data availability

The experimental and simulated data that support the findings of this study are available from the corresponding authors upon request.

### Code availability

The codes used in this work are available from the corresponding authors upon request.

## Acknowledgements

We acknowledge T. N. Shendruk, A. Doostmohammadi, K. Thijssen and J. M. Yeomans for providing the dataset<sup>29</sup> analysed in Supplementary Fig. 3. We are grateful to S. Shankar and N. Molinari for helpful discussions. This work is partially supported by the Schmidt Science Fellowship and the Postdoc Mobility Fellowship from the Swiss National Foundation (M.S.); the Netherlands Organization for Scientific Research (NWO/OCW) as part of the Frontiers of Nanoscience program and the Vidi scheme (L.G.); the Department of Energy, Office of Basic Energy Sciences, under award no. DESC0019733 (Z.D.); and the NSF Simons Center for Mathematical and Statistical Analysis of Biology via award no. 1764269 (L.M.).

## Author contributions

M.S. and L.M. designed research, M.S. performed the research. M.S., L.L., L.G., Z.D. and L.M. contributed to the new experimental, numerical and analytical tools. M.S., L.L., L.G., Z.D. and L.M. analysed the data, and M.S. and L.M. wrote the manuscript. All authors commented on the manuscript.

## Competing interests

The authors declare no competing interests.

## Additional information

**Supplementary information** The online version contains supplementary material available at <https://doi.org/10.1038/s41567-023-02062-y>.

**Correspondence and requests for materials** should be addressed to Mattia Serra or L. Mahadevan.

**Peer review information** *Nature Physics* thanks the anonymous reviewers for their contribution to the peer review of this work

**Reprints and permissions information** is available at [www.nature.com/reprints](http://www.nature.com/reprints).